European Polymer Journal 230 (2025) 113906

Contents lists available at ScienceDirect

European Polymer Journal

journal homepage: www.elsevier.com/locate/europolj

Polyolefin based Nano-Objects via ARGET ATRP mediated Polymerization-Induced Self-Assembly process

Xinyue Liang, Jingwei Zhang, Xiaoxiao Wu, Xiaotong Fang, Pengyu Qu, Guowei Wang *

State Key Laboratory of Molecular Engineering of Polymers, Department of Macromolecular Science, Fudan University, Shanghai 200433, China

ARTICLE INFO

Keywords:
Activator regenerated by electron transfer atom transfer radical polymerization (ARGET ATRP)
Polymerization-induced self-assembly (PISA)
Polyolefin based nano-objects

ABSTRACT

Polyolefins (POs) are key materials in industrial applications, and the development of high-performance and high-value-added POs is always a significant and challenging research focus. The major challenge lies in addressing compatibility between non-polar POs and polar functional components. We herein reported a facile strategy to prepare PO-based nano-objects using an activator regenerated by electron transfer atom transfer radical polymerization mediated polymerization-induced self-assembly (ARGET ATRP PISA) process based on hydrogenated polyisoprene-*b*-poly (glycidyl methacrylate) (HPI-*b*-PGMA)/poly (glycidyl methacrylate) (PGMA) blends. The dynamic light scattering (DLS) and transmission electron microscopy (TEM) revealed effective control over a wide range of hydrodynamic diameters of stabilized spherical nano-objects. The thermogravimetric analysis (TGA) and microscale combustion calorimetry (MCC) demonstrated the efficient and controllable introduction of phosphoric acid (H_3PO_4) into nano-objects, with POs serving as the shell and flame retardants forming the core. This work was hoped to provide a versatile route to PO-based nano-objects and open a novel avenue for designing PO-based additives.

1. Introduction

Polyolefins (POs), including crystallizable polyethylene (PE), polypropylene (PP), and non-crystallizable polyolefin elastomer (POE), ethylene propylene diene monomer (EPDM) rubber, ethylene–vinyl acetate (EVA) copolymer, *etc.*, have attracted significant attention due to their excellent mechanical properties, chemical stability, ease of processing, availability of raw materials, cost-effectiveness, and diverse applications [1,2]. However, the growing demand for advanced materials has posed significant challenges in the POs industry, particularly in functionalized POs. For example, the inherently low miscibility between POs and polar additives (such as antioxidants, flame retardants, photostabilizers, etc.) consistently hinders property enhancement. Specifically, during the processing, storage, and application, the polar additives tend to migrate out of the PO matrix, leading to material degradation [3,4,5].

To address these issues, the researchers have attempted to introduce the polar functional groups into PO chains through post-polymerization modification, and to impart new functionalities while preserving their inherent excellent properties [6]. For example, Bunescu *et al.* used *meta*-chloroperbenzoic acid to hydroxylate PE, thereby producing polymers suitable for graft copolymer preparation [7]. Gao *et al.* realized the copolymerization of ethylene with polar comonomers containing phosphorus, silicon, and boron using a phosphorus-sulfonate palladium catalyst [8]. Zou *et al.* developed an efficient method to produce polar-functionalized, cross-linkable, self-healing, and photo-responsive POs with thermoplastic, elastomeric, and thermosetting properties by incorporating tunable carboxylic acids and cyclic comonomers through palladium-catalyzed ternary polymerization of ethylene, ethylidene norbornene (ENB) and methyl 10-undecenoate [9]. These copolymers can be directly used in some advanced applications or serve as compatibilizers for PO blends [6]. However, due to the chemical inertness and low surface energy of POs, as well as the expensive catalyst, effectively incorporating polar units into the copolymer chain remains a critical challenge in the development of functional POs [10]. Additionally, the applications of functionalized POs are still limited in certain areas.

Alternatively, the PO segments can be immobilized onto the periphery of nano-objects, which serve as additives in the PO industry. The PO-based nano-objects could significantly enhance compatibility by optimizing interactions between PO and functional additive components at the nanoscale, thereby improving the overall material performance. Over the past two decades, the advancements in “living”/controlled

---

* Corresponding author.
E-mail address: gwwang@fudan.edu.cn (G. Wang).

https://doi.org/10.1016/j.eurpolymj.2025.113906
Received 20 December 2024; Received in revised form 16 March 2025; Accepted 22 March 2025

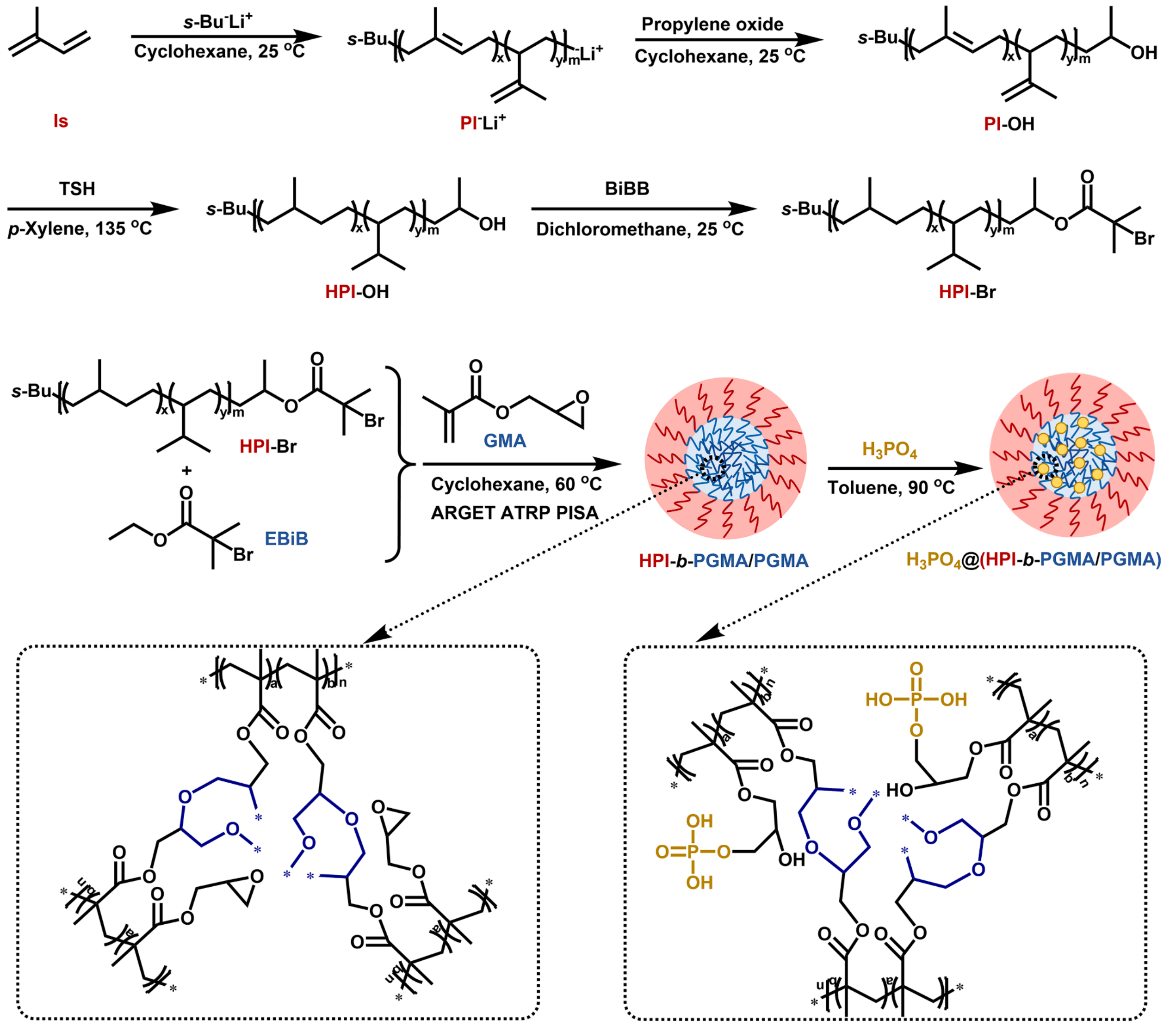

Scheme 1. The synthetic procedure for HPI-*b*-PGMA/PGMA based nano-objects via ARGET ATRP PISA and H_3PO_4@(HPI-*b*-PGMA/PGMA) based nano-objects via ring-opening reaction.

polymerization mechanisms, including reversible addition-fragmentation chain transfer (RAFT) polymerization [11,12], nitroxide-mediated radical polymerization (NMRP) [13,14], atom transfer radical polymerization (ATRP) [15], living anionic polymerization (LAP) [16,17] and ring-opening metathesis polymerization (ROMP) [18,19], have accelerated extensive research on self-assembly technique. The self-assembly systems in solution have evolved from a traditional dilute solution system (<1.0 % *w/w*) to a high solid content (up to 50 % *w/w*) polymerization-induced self-assembly (PISA) system. Typically, the PISA approach employed a solvophilic polymer as the stabilizer, inducing the formation of block copolymer and *in-situ* self-assembly process during the polymerization of the second monomer [20,21]. Additionally, by exploring unique polymer–solvent interactions, the derived approaches such as polymerization-induced cooperative assembly (PICA), polymerization-induced chiral self-assembly (PICSA), and polymerization-induced interfacial self-assembly (PIISA), *etc*., have also emerged [22]. For example, Zhu *et al.* proposed a PICA system, which involves the simultaneous use of a solvophilic macromolecular chain transfer agent (macro-CTA) and a small-molecular CTA in the PISA process to form colloidally stable nano-objects composed of well-defined block copolymer and homopolymer [23]. Such a PICA process effectively accelerated the morphological transitions toward higher-order morphologies [24,25] and was highly effective in tuning the size of spheres [24]. Generally, in PISA or the derived approaches, the final morphologies are primarily dictated by the employed blocks and solvents, as expressed by the packing parameter $P = v/a_0l_c$ (v, a_0, and l_c represent the volume of core-forming block, the interfacial area, and the length of core-forming block, respectively) [20,26]. Thus, the self-assembly offers a promising approach for preparing nano-objects, significantly advancing their applications [27,28]. However, up to now, most PISA systems focus on poly[(methyl)acrylate], polystyrenes, polylactones, and polycycloolefins [15,19,20], and limited systems on POs were reported. For example, D’Agosto *et al.* have ever synthesized the poly(ethylene oxide)-*b*-poly(ethylene) (PEO-*b*-PE) based nano-objects using RAFT PISA approach [29]. Using the coordinative chain-transfer polymerization, they also prepared the poly(ethylene-*co*-butadiene)-*b*-poly(ethylene) based nano-objects [30]. In these two cases, the crystallization-driven self-assembly (CDSA) mechanism [31,32,33,34] was indeed involved and the crystallizable PE was designed as the core. In fact, the crystallizable PE or PP based POs were always constrained by the complex stereoregular structures and challenging dissolution behaviors, as well as the difficulty in synthesizing copolymers with PO segment-containing topologies. Alternatively, using the non-crystallizable POs as the stabilizer, Armes *et al.* reported the first example of the hydrogenated polybutadiene-*b*-poly(benzyl methacrylate) (PhBD-*b*-PBZMA) based nano-objects via RAFT PISA, achieving the spherical, worm-like, and vesicular micelles under high concentrations up to 40–45 % *w/w* in non-polar media [35]. Nevertheless, the extensive preparation of PO-based nano-objects and exploration on their applications are still urgent.

Inspired by the potential applications of PO-based nano-objects and the present research progress, herein, we designed some hydrogenated polyisoprene-*b*-poly(glycidyl methacrylate) (HPI-*b*-PGMA) based and HPI-*b*-PGMA/PGMA based nano-objects via activator regenerated by electron transfer atom transfer radical polymerization-mediated polymerization-induced self-assembly (ARGET ATRP PISA) process (Scheme 1). Specifically, the process started with the LAP of isoprene (Is) initiated by *sec*-butyllithium (s-Bu$^-$Li$^+$), followed by termination with 1,2-epoxypropane and complete hydrogenation using 4-methylbenzenesulfonhydrazide (TSH) agent, and the preparation of ATRP macroinitiator HPI-Br through esterification with 2-bromo-isobutyryl bromide (BiBB). Subsequently, the HPI-Br and ethyl 2-bromoisobutyrate (EBiB) synergistically initiated the polymerization of glycidyl methacrylate (GMA) in cyclohexane to achieve ARGET ATRP PISA process. Notably, the stannous octoate ($\mathrm{SnOct_2}$) acted both as a catalyst in ARGET ATRP process and ring-opening process of oxirane groups, which facilitated the *in-situ* crosslinking and stabilization of nano-objects [36]. The hydrodynamic diameter of the nano-objects was modulated by adjusting the molar ratio of $[\mathrm{EBiB}]_0/[\mathrm{HPI\text{-}Br}]_0$ and the degree of polymerization of PGMA ($\mathrm{DP_{PGMA}}$). Furthermore, the PGMA core in nano-objects was modified with phosphoric acid ($\mathrm{H_3PO_4}$), proposing the potential application in enhancing the flame resistance of non-crystallizable PO-based materials.

2. Experimental

2.1. Materials and characterization

Isoprene (Is, 99 %, TCI) and 1,2-epoxypropane (99 %, TCI) were dried over $\mathrm{CaH_2}$, distilled and stored in a refrigerator below 4 ℃. Cyclohexane (99 %, Adamas) was dried over $\mathrm{CaH_2}$ and distilled prior to use. Dichloromethane (DCM, ≥99.5 %, Tansoole) was dried over $\mathrm{CaH_2}$, distilled and stored in a refrigerator below 4 ℃. Glycidyl methacrylate (GMA, 99 %, Adamas) was purified by aluminium (III) oxide (alkaline 200–300 mesh, Tansoole). s-Butyllithium (s-Bu$^-$Li$^+$, 1.3 M in n-hexane, Aladdin), n-butyllithium (n-Bu$^-$Li$^+$, 1.6 M in n-hexane, Adamas), 4-methylbenzenesulfonhydrazide (TSH, 98 %, Adamas), p-xylene (PX, ≥99.0 %, Tansoole), 2-bromo-2-methylpropionyl bromide (BiBB, 98 %, Adamas), triethylamine (≥99 %, Tansoole), ethyl 2-bromoisobutyrate (EBiB, 98 %, Adamas), cupric bromide ($\mathrm{CuBr_2}$, 99 %, Adamas), tris[2-(dimethylamino)ethyl]amine ($\mathrm{Me_6TREN}$, 97 %, Adamas), stannous octoate ($\mathrm{SnOct_2}$, 95 %, Adamas) and phosphoric acid ($\mathrm{H_3PO_4}$, 85 %, Adamas) were used as received. All other reagents were purchased from Sinopharm Chemical Reagent Co. (SCRC) and used as received except for additional declaration.

The characterization methods were shown in the Supporting Information.

2.2. Preparation of ATRP macroinitiator HPI-Br

Firstly, the PI-OH was synthesized via a LAP process. Dried cyclohexane (215.2 mL, 2.02 mol) and isoprene (44.2 mL, 0.44 mol) were sequentially introduced into a 500 mL pre-baked and vacuum-sealed flask filled with nitrogen. The impurities in the mixture were pre-consumed by adding s-Bu$^-$Li$^+$, followed by the rapid addition of the metered initiator s-Bu$^-$Li$^+$ (6.70 mL, 6.03 mmol) to initiate polymerization. After 24 h, 0.40 mL of the mixture was withdrawn for characterization. Into a 20 mL pre-baked and vacuum-sealed flask filled with nitrogen, dried cyclohexane (5.00 mL, 46.34 mmol) and 1,2-epoxypropane (5.00 mL, 72.31 mmol) were sequentially introduced. The impurities in the mixture were pre-consumed by the addition of n-Bu$^-$Li$^+$. When the solution turned light yellow and remained unchanged for 5 min, it was quickly transferred into above polymerization system. After another 24 h, the methanol (0.10 mL, 2.46 mmol) was added. The synthesized PI-OH was purified by precipitation into methanol three times and dried in a vacuum oven for further experiment. (Yield: 28.30 g, 94.33 %) PI, SEC: $M_{\mathrm{n,SEC}} = 6{,}800$ g/mol, $M_w/M_n = 1.05$. ^{1}H NMR ($\mathrm{CDCl_3}$, δ, ppm, TMS): 0.88 (t, $\mathrm{C}\boldsymbol{H}_3\mathrm{CH_2}$–), 0.94 (d, $\mathrm{CH_3CH_2(C}\boldsymbol{H}_3\mathrm{)CH}$–), 1.22 – 2.25 (m, aliphatic main chain –$\mathrm{C}\boldsymbol{H}_2\mathrm{C}\boldsymbol{H}$-, –$\mathrm{C}\boldsymbol{H}_2\mathrm{C}\boldsymbol{H}_2$-), 1.86 (m, –$\mathrm{C(C}\boldsymbol{H}_3\mathrm{){=}CH}$– of 1,4-addition, –$\mathrm{C(C}\boldsymbol{H}_3\mathrm{){=}CH_2}$ of 3,4-addition), 4.50 – 4.90 (–$\mathrm{(CH_3)C{=}C}\boldsymbol{H}_2$ of 3,4-addition), 5.12 (–$\mathrm{C}\boldsymbol{H}\mathrm{{=}C(CH_3)}$- of 1,4-addition). PI-OH, SEC: $M_{\mathrm{n,SEC}} = 7{,}000$ g/mol, $M_w/M_n = 1.05$. ^{1}H NMR ($\mathrm{CDCl_3}$, δ, ppm, TMS): 0.88 (t, $\mathrm{C}\boldsymbol{H}_3\mathrm{CH_2}$–), 0.94 (d, $\mathrm{CH_3CH_2(C}\boldsymbol{H}_3\mathrm{)CH}$–), 1.17 (d, –$\mathrm{CH_2(C}\boldsymbol{H}_3\mathrm{)CHO}$–), 1.22 – 2.25 (m, aliphatic main chain –$\mathrm{C}\boldsymbol{H}_2\mathrm{C}\boldsymbol{H}$-, –$\mathrm{C}\boldsymbol{H}_2\mathrm{C}\boldsymbol{H}_2$-), 1.86 (m, –$\mathrm{C(C}\boldsymbol{H}_3\mathrm{){=}CH}$– of 1,4-addition, –$\mathrm{C(C}\boldsymbol{H}_3\mathrm{){=}CH_2}$ of 3,4-addition), 3.78 (qd, –$\mathrm{CH_2(CH_3)C}\boldsymbol{H}\mathrm{O}$–), 4.50 – 4.90 (–$\mathrm{(CH_3)C{=}C}\boldsymbol{H}_2$ of 3,4-addition), 5.12 (–$\mathrm{C}\boldsymbol{H}\mathrm{{=}C(CH_3)}$- of 1,4-addition).

Secondly, the HPI-OH was synthesized through a hydrogenation process. Typically, PI-OH (9.40 g, 1.34 mmol) was dissolved in PX (62.2 mL, 0.50 mol), and TSH (5.14 g, 27.60 mmol) and added into a 250 mL flask. After refluxing at 135 ℃ for 15 min, the TSH (5.14 g, 27.60 mmol) was added every 15 min for a total of 102.80 g (four times of the double bond). After the final addition, the mixture was refluxed for an additional 30 min to complete the reaction. The HPI-OH was purified three times from a mixed solution of sodium hydroxide in methanol and water (pH of 11), and dried in a vacuum oven for further experiment. (Yield: 9.20 g, 94.94 %) HPI-OH, SEC: $M_{\mathrm{n,SEC}} = 7{,}600$ g/mol, $M_w/M_n = 1.06$. ^{1}H NMR ($\mathrm{CDCl_3}$, δ, ppm, TMS): 0.50–0.95 (m, $\mathrm{C}\boldsymbol{H}_3\mathrm{CH_2}$–, –$\mathrm{C}\boldsymbol{H}_2\mathrm{(C}\boldsymbol{H}_3\mathrm{)C}\boldsymbol{H}$–, –$\mathrm{CH(C}\boldsymbol{H}_3\mathrm{)_2}$), 0.96–1.80 (m, $\mathrm{CH_3C}\boldsymbol{H}_2\mathrm{(C}\boldsymbol{H}_3\mathrm{)C}\boldsymbol{H}$–, –$\mathrm{C}\boldsymbol{H}_2\mathrm{C}\boldsymbol{H}_2$-, –$\mathrm{C}\boldsymbol{H}\mathrm{(CH_3)_2}$, –$\mathrm{C}\boldsymbol{H}_2\mathrm{C}\boldsymbol{H}$-, $\mathrm{C}\boldsymbol{H}_2\mathrm{(C}\boldsymbol{H}_3\mathrm{)CHO}$–), 3.78 (qd, –$\mathrm{CH_2(CH_3)C}\boldsymbol{H}\mathrm{O}$–).

Finally, the HPI-Br was synthesized through an esterification process. The HPI-OH (11.60 g, 1.53 mmol) was firstly dissolved in toluene (250.0 mL, 2.36 mol) in a 500 mL flask and distilled at 140 ℃ to remove trace water by an azeotropic distillation process. After the flask was cooled to room temperature, dry triethylamine (4.60 mL, 33.18 mmol) and DCM (210.1 mL, 3.29 mol) were added. Subsequently, the BiBB (2.30 mL, 18.61 mmol) was added dropwise under an ice water bath. After the addition was complete, the ice water bath was removed, and the reaction proceeded at room temperature for 72 h. The HPI-Br was purified three times from methanol, dried in a vacuum oven, and stored in a refrigerator below 4 ℃ for further experiment. (Yield: 11.25 g, 95.09 %) HPI-Br, SEC: $M_{\mathrm{n,SEC}} = 8{,}600$ g/mol, $M_w/M_n = 1.06$. ^{1}H NMR ($\mathrm{CDCl_3}$, δ, ppm, TMS): 0.50–0.95 (m, $\mathrm{C}\boldsymbol{H}_3\mathrm{CH_2}$–, –$\mathrm{C}\boldsymbol{H}_2\mathrm{(C}\boldsymbol{H}_3\mathrm{)C}\boldsymbol{H}$–, –$\mathrm{CH(C}\boldsymbol{H}_3\mathrm{)_2}$), 0.96–1.80 (m, $\mathrm{CH_3C}\boldsymbol{H}_2\mathrm{(C}\boldsymbol{H}_3\mathrm{)C}\boldsymbol{H}$–, –$\mathrm{C}\boldsymbol{H}_2\mathrm{C}\boldsymbol{H}_2$-, –$\mathrm{C}\boldsymbol{H}\mathrm{(CH_3)_2}$, –$\mathrm{C}\boldsymbol{H}_2\mathrm{C}\boldsymbol{H}$-, $\mathrm{C}\boldsymbol{H}_2\mathrm{(C}\boldsymbol{H}_3\mathrm{)CHO}$–), 1.80 (s, –$\mathrm{C(C}\boldsymbol{H}_3\mathrm{)_2Br}$), 3.88 (qd, –$\mathrm{CH_2(CH_3)C}\boldsymbol{H}\mathrm{O}$–).

2.3. Preparation of HPI-b-PGMA/PGMA based nano-objects via ARGET ATRP PISA process

As an example, the $\mathrm{HPI_{107}}$-*b*-$\mathrm{PGMA_{40}/PGMA_{40}}$ based nano-objects with a solids content of 20 % *w/w* were prepared. Firstly, HPI-Br (0.5000 g, 0.0581 mmol), EBiB (0.0113 g, 0.0581 mmol), GMA (0.6612 g, 4.6512 mmol), $\mathrm{CuBr_2}$ (0.0010 g, 0.0046 mmol), $\mathrm{Me_6TREN}$ (0.0022 g, 0.0092 mmol), and cyclohexane (5.95 mL, 55.19 mmol) were sequentially added into a 10 mL flask. After bubbling with nitrogen for 30 min, the flask was placed into an oil bath at 60 ℃ for 15 min. Then, the $\mathrm{SnOct_2}$ (0.0372 g, 0.0920 mmol) was added to initiate the reaction. The polymerization was continued for 24 h, gradually forming the dispersion, and the ARGET ATRP PISA process was achieved. $\mathrm{HPI_{107}}$-*b*-$\mathrm{PGMA_{40}/PGMA_{40}}$, ^{1}H NMR ($\mathrm{CDCl_3}$, δ, ppm, TMS): 0.50–0.95 (m, $\mathrm{C}\boldsymbol{H}_3\mathrm{CH_2}$–, –$\mathrm{C}\boldsymbol{H}_2\mathrm{(C}\boldsymbol{H}_3\mathrm{)C}\boldsymbol{H}$–, –$\mathrm{CH(C}\boldsymbol{H}_3\mathrm{)_2}$), 0.96–1.80 (m, $\mathrm{CH_3C}\boldsymbol{H}_2\mathrm{(C}\boldsymbol{H}_3\mathrm{)C}\boldsymbol{H}$–, –$\mathrm{C}\boldsymbol{H}_2\mathrm{C}\boldsymbol{H}_2$-, –$\mathrm{C}\boldsymbol{H}\mathrm{(CH_3)_2}$, –$\mathrm{C}\boldsymbol{H}_2\mathrm{C}\boldsymbol{H}$-, $\mathrm{C}\boldsymbol{H}_2\mathrm{(C}\boldsymbol{H}_3\mathrm{)CHO}$–, –$\mathrm{CH_2C(C}\boldsymbol{H}_3\mathrm{)}$-, –$\mathrm{C(C}\boldsymbol{H}_3\mathrm{)_2}$-), 1.80–2.20 (d, –$\mathrm{C}\boldsymbol{H}_2\mathrm{C}$-), 2.53–2.93 (m, –$\mathrm{C}\boldsymbol{H}_2\mathrm{O}$- on epoxy group), 3.24 (–$\mathrm{C}\boldsymbol{H}\mathrm{(CH_2}$–$\mathrm{)O}$-), 3.70–4.40 (d, –$\mathrm{COOC}\boldsymbol{H}_2$- on PGMA), 3.88 (qd, –$\mathrm{CH_2(CH_3)C}\boldsymbol{H}\mathrm{O}$–).

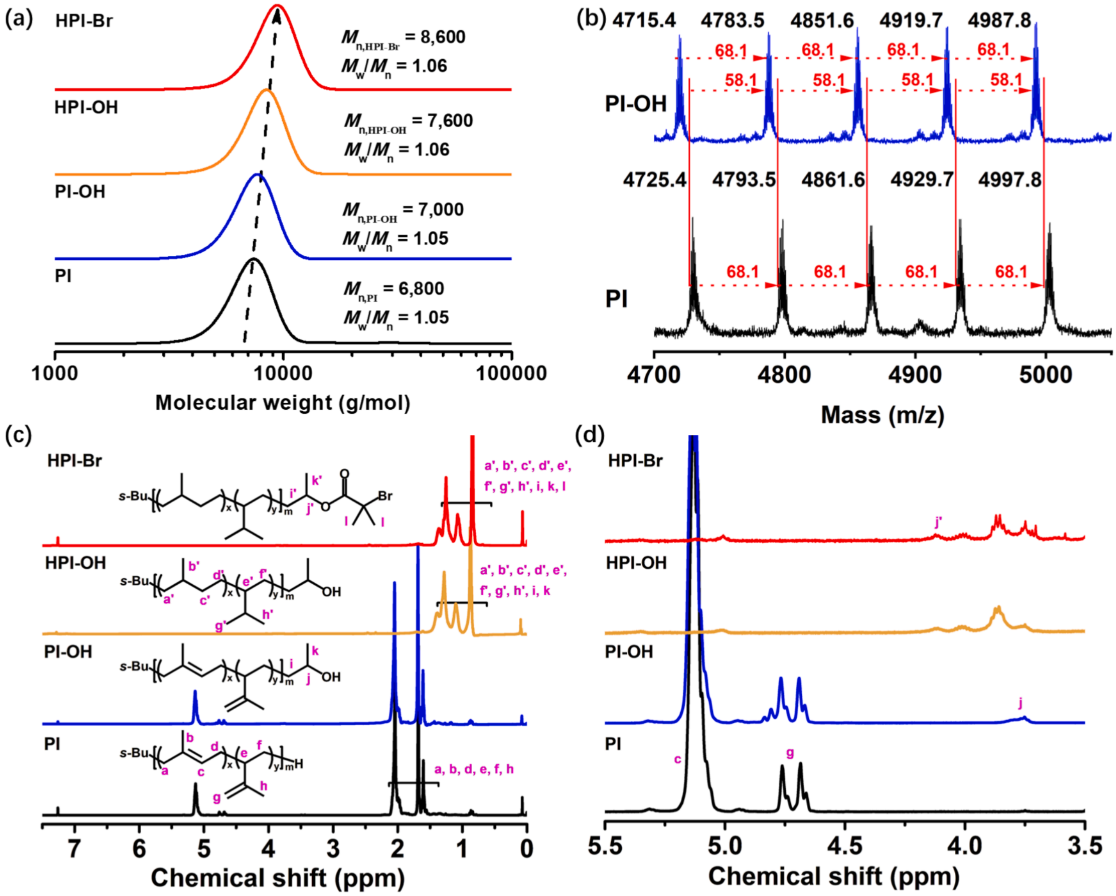

Fig. 1. (a) SEC traces for PI, PI-OH, HPI-OH and HPI-Br (using THF as eluent and PS as standard). (b) MALDI-TOF MS for PI and PI-OH. (c, d) ^{1}H NMR spectra for PI, PI-OH, HPI-OH and HPI-Br, spectrum (d) is a magnified view of spectrum (c) in the region of 5.5–3.5 ppm, in $CDCl_3$.

2.4. Preparation of H_3PO_4@(HPI-b-PGMA/PGMA) nano-objects

Using the preparation of H_3PO_4@(HPI_{107}-*b*-$PGMA_{40}$/$PGMA_{40}$) as an example, the HPI_{107}-*b*-$PGMA_{40}$/$PGMA_{40}$ (0.5000 g, 0.0250 mmol) nano-objects were purified three times from methanol and then redispersed in THF (10.60 mL, 0.13 mol) in a 50 mL flask. After the addition of H_3PO_4 (0.32 mL, 4.65 mol), the mixture was refluxed at 90 ℃ for 8 h. The excess H_3PO_4 was washed using methanol, and the H_3PO_4@(HPI_{107}-*b*-$PGMA_{40}$/$PGMA_{40}$) nano-objects were obtained.

3. Results and Discussion

3.1. Synthesis and characterization of ATRP macroinitiator HPI-Br

Using the LAP process of Is monomer and subsequent functionalization of terminal living species PI^-Li^+ with 1,2-epoxypropane, the hydroxyl-terminated PI-OH was first synthesized. Following the method in the literature [37], the PI-OH was hydrogenated using TSH agent, yielding HPI-OH. The terminal hydroxyl groups were further converted into bromide groups via efficient esterification with BiBB agent, resulting in the ATRP macroinitiator HPI-Br. The successful synthesis of PI, PI-OH, HPI-OH, and HPI-Br was comprehensively characterized using proton nuclear magnetic resonance (^{1}H NMR), size exclusion chromatography (SEC), and matrix-assisted laser desorption ionization time of flight mass spectrometry (MALDI-TOF MS), respectively.

As the SEC curves shown in Fig. 1**a**, the PI synthesized via the LAP process exhibited a narrow molecular weight distribution (MWD). Following the terminal functionalization and hydrogenation, the derived PI-OH, HPI-OH, and HPI-Br also maintained narrow MWDs. Notably, the number-average molecular weight (M_n) increased slightly and consistently after each modification step. According to the SEC results for HPI-OH, the DP of HPI-OH (DP_{HPI}) was calculated as 107. The structures of PI and PI-OH were further confirmed by MALDI-TOF MS. As the enlarged MALDI-TOF MS shown in Fig. 1**b**, after end-capping of PI^-Li^+ with 1,2-epoxypropane, the peak 4793.5 Da assigned to the PI (C_4H_9-$(C_5H_8)_{68}$-HAg^+) shifted to the peak 4851.6 Da (C_4H_9-$(C_5H_8)_{68}$-C_3H_6-$OHAg^+$) assigned to the PI-OH. Clearly, the difference of 58.1 Da (Δm = 4851.6 – 4793.5 = 58.1 Da) corresponded to the mass of a 1,2-epoxypropane unit. These results exhibited an isotope pattern that aligned with the theoretical one from isotopic distribution simulations (**Fig. S1**). The absence of any additional signals in MALDI-TOF MS supported the high end-capping efficiency. Furthermore, from the ^{1}H NMR spectra for PI (Fig. 1**c** and Fig. 1**d**), the characteristic resonance signal for alkene protons ($-C(CH_3)=C\boldsymbol{H}-$) on 1,4-addition Is unit appeared at 5.12 ppm, while the signal for alkene protons ($-C(CH_3)=C\boldsymbol{H_2}$) on the 3,4-addition Is unit appeared between 4.50 and 4.90 ppm. According to the ^{1}H NMR spectra, the contents of 1,4-addition and 3,4-addition Is units on PI were calculated as 94.8 % and 5.2 %, respectively. For ^{1}H NMR spectra of PI-OH, the methine proton ($-CH_2C\boldsymbol{H}(CH_3)OH$) connected to the hydroxyl group appeared at 3.70 ppm, combining the resonance signal in the range of 0.70–1.00 ppm for methyl protons ($C\boldsymbol{H_3}CH_2(C\boldsymbol{H_3})CH-$) on two terminal methyl groups of the *sec*-butyl residual, the epoxy end-capping efficiency was determined as 96.5 %. Based on the integral areas corresponding to the resonance signal at 5.12 ppm ($-C(CH_3)=C\boldsymbol{H}-$), 4.50–4.90 ppm ($-C(CH_3)=C\boldsymbol{H_2}$), and 0.70–1.00 ppm ($C\boldsymbol{H_3}CH_2(C\boldsymbol{H_3})CH-$) in the ^{1}H NMR spectrum (**Fig. S2**), the $M_{n,NMR}$ of PI-OH was derived as 6500 g/mol, which was close to the $M_{n,SEC}$ of 7000 g/mol for PI-OH. For ^{1}H NMR spectra of HPI-OH, the signals assigned to the alkene protons between 4.25–5.40 ppm disappeared completely, indicating 100 % hydrogenation of the PI main chain. For

Table 1
Formulation and characterization for HPI-*b*-PGMA/PGMA based nano-objects with varied wt$_{PGMA}$/wt$_{HPI}$ and [EBiB]$_0$/[HPI-Br]$_0$ ratios. [a].

Samples[b]	wt$_{PGMA}$/ wt$_{HPI}$[c]	[EBiB]$_0$/ [HPI-Br]$_0$	Hydrodynamic Diameter (nm)[d] Tetrahydrofuran (THF)	Cyclohexane (CH)
HPI$_{107}$-*b*-PGMA$_{40}$	0.74	0	122	68
HPI$_{107}$-*b*-PGMA$_{20}$/PGMA$_{20}$	0.74	1.0	255	141
HPI$_{107}$-b-PGMA$_{13}$/PGMA$_{13}$	0.74	2.0	295	190
HPI$_{107}$-b-PGMA$_{8}$/PGMA$_{8}$	0.74	4.0	341	255
HPI$_{107}$-*b*-PGMA$_{4}$/PGMA$_{4}$	0.74	8.0	396	255
HPI$_{107}$-*b*-PGMA$_{80}$	1.47	0	105	68
HPI$_{107}$-*b*-PGMA$_{40}$/PGMA$_{40}$	1.47	1.0	295	164
HPI$_{107}$-*b*-PGMA$_{26}$/PGMA$_{26}$	1.47	2.0	341	220
HPI$_{107}$-*b*-PGMA$_{16}$/PGMA$_{16}$	1.47	4.0	396	341
HPI$_{107}$-*b*-PGMA$_{8}$/PGMA$_{8}$	1.47	8.0	531	396
HPI$_{107}$-*b*-PGMA$_{120}$	2.21	0	141	105
HPI$_{107}$-*b*-PGMA$_{60}$/PGMA$_{60}$	2.21	1.0	396	164
HPI$_{107}$-*b*-PGMA$_{40}$/PGMA$_{40}$	2.21	2.0	458	190
HPI$_{107}$-*b*-PGMA$_{24}$/PGMA$_{24}$	2.21	4.0	531	458
HPI$_{107}$-*b*-PGMA$_{13}$/PGMA$_{13}$	2.21	8.0	Precipitate	
HPI$_{107}$-*b*-PGMA$_{160}$	2.95	0	164	91
HPI$_{107}$-*b*-PGMA$_{80}$/PGMA$_{80}$	2.95	1.0	Precipitate	
HPI$_{107}$-*b*-PGMA$_{320}$	5.90	0	164	91

[a] The solids content was fixed as 20 % *w/w*. [b] The subscript represented the DP of PGMA block in HPI-*b*-PGMA and PGMA homopolymer, respectively, which was calculated according to the complete conversion of GMA monomer derived by ^{1}H NMR spectrum and the designed [EBiB]$_0$/[HPI-Br]$_0$ ratios. [c] The wt$_{PGMA}$/wt$_{HPI}$ ratio was calculated based on the weight ratio of the fed GMA monomer to the macroinitiator HPI-Br. [d] The hydrodynamic diameter was evaluated by the DLS measurement using tetrahydrofuran (THF) or cyclohexane (CH) as solvent.

^{1}H NMR spectra of HPI-Br, the methine proton (–CH$_2$C***H***(CH$_3$)OO–) connected to the ester linkage appeared at 3.88 ppm, and the methyl protons (−C(C***H***$_3$)$_2$Br) overlapped at 1.68–1.90 ppm with that for methylene protons (–C***H***$_2$CH(CH$_3$)O-. Combining the ^{1}H NMR spectra for HPI-OH and HPI-Br, the overall bromination efficiency was calculated as 92.1 % by analyzing the change in the integral area between 1.68–1.90 ppm for protons (–C***H***$_2$CH(CH$_3$)O-) before the bromination, and the that for protons (−C(C***H***$_3$)$_2$Br) after bromination (**Fig. S3 and S4**). In general, the SEC, MALDI-TOF MS, and ^{1}H NMR spectra comprehensively provided solid evidence that the ATRP macroinitiator HPI-Br has been successfully prepared and could be employed in the subsequent ARGET ATRP PISA process.

3.2. Preparation of HPI-b-PGMA/PGMA based nano-objects via ARGET ATRP PISA process

Our previous work [24] and the literatures [38,39] indicated that the size of nano-objects in the PISA process could be modulated by introducing the small-molecular initiators. Thus, herein, employing the ARGET ATRP PISA process, the HPI-*b*-PGMA/PGMA based nano-objects were targeted by using HPI-Br as macroinitiator (as well as stabilizer), EBiB as small-molecular initiator, GMA as monomer, cyclohexane as solvent, cupric bromide/tris[2-(dimethylamino)ethyl]amine (CuBr$_2$/Me$_6$TREN) complex as catalyst, and SnOct$_2$ as reducing agent. Specifically, the solids content was maintained at 20 % *w/w*, and the DP of the macroinitiator HPI-Br was fixed at 107. The wt$_{PGMA}$/wt$_{HPI}$ ratios were set as 0.74, 1.47, 2.21, 2.95, 5.90, corresponding to the formation of HPI-*b*-PGMA with DP$_{PGMA}$s of 40, 80, 120, 160, 320, respectively. It should be mentioned that the polymerization of GMA monomer during the ARGET ATRP PISA process could be divided into three stages. The first stage was a slow polymerization in a homogeneous solution. Although cyclohexane was not a good solvent for small molecular initiator EBiB, CuBr$_2$/Me$_6$TREN catalyst and Sn(Oct)$_2$ reducing agent, the GMA monomer itself served as the cosolvent and the initiation of ATRP could smoothly happened at this stage, which could also be confirmed by the homogeneous solution in the initial stage. Later, the second stage could be attributed to a faster polymerization in the micelles formed by aggregation of the generated diblock copolymers. The GMA monomer in the micelles enhanced the local monomer concentration and accelerated the polymerization rate at this stage. Due to the close polarity between CuBr$_2$/Me$_6$TREN catalyst, Sn(Oct)$_2$ reducing agent and GMA monomer, the additives tended to be encapsuled in the core region. Finally, in the third stage, the GMA monomer was completely converted, and the ring-opening polymerization was accompanied. Thus, based on the above analysis on AREGT ATRP PISA process, either by the enhanced solubility with GMA monomer or the unique PISA process, the solubility of CuBr$_2$/Me$_6$TREN catalyst and Sn (Oct)$_2$ reducing agent in cyclohexane was improved and the polymerization could be smoothly performed.

Furthermore, by varying the [EBiB]$_0$/[HPI-Br]$_0$ ratios, the HPI-*b*-PGMA/PGMA with different content of PGMA homopolymer could be generated, and the sizes of the nano-objects were thus modulated (Table 1). Regularly, in the cases with relatively lower wt$_{PGMA}$/wt$_{HPI}$s ratios of 0.74 and 1.47, the nano-objects could all be well stabilized in non-polar cyclohexane by varying the [EBiB]$_0$/[HPI-Br]$_0$ ratios. However, in the case with wt$_{PGMA}$/wt$_{HPI}$s ratio of 2.21, the precipitate occurred when [EBiB]$_0$/[HPI-Br]$_0$ ratio was increased to 8.0. Especially, in the case with wt$_{PGMA}$/wt$_{HPI}$s ratio of 2.95, the precipitate even happened when [EBiB]$_0$/[HPI-Br]$_0$ ratio was increased to 1.0. The higher wt$_{PGMA}$/wt$_{HPI}$s and [EBiB]$_0$/[HPI-Br]$_0$ ratios favored the precipitates, the reason could be attributed to the increased diameters, and correspondingly, the reduced stability of nano-objects.

The previous literature demonstrated that the oxirane group on PGMA could be further polymerized and crosslinked in the presence of SnOct$_2$ agent, which either occurred as an undesired side reaction [36] or could be controlled in a specific manner [40,41]. Thus, the ring-opening reaction of the oxirane group allowed for *in-situ* crosslinking of the PGMA core and the generation of stabilized nano-objects. Especially, our previous work has shown that the ring-opening polymerization of the oxirane ring was slower than the radical polymerization of the double bond on the GMA monomer [36], which facilitated a first PISA process and a second crosslinking reaction. Due to the presence of a ring-opening reaction and the corresponding crosslinking reaction, the generated products could not be solubilized in any solvents and analyzed by SEC measurement. Alternatively, according to the ^{1}H NMR spectrum, the resonance signals attributed to the double bond protons

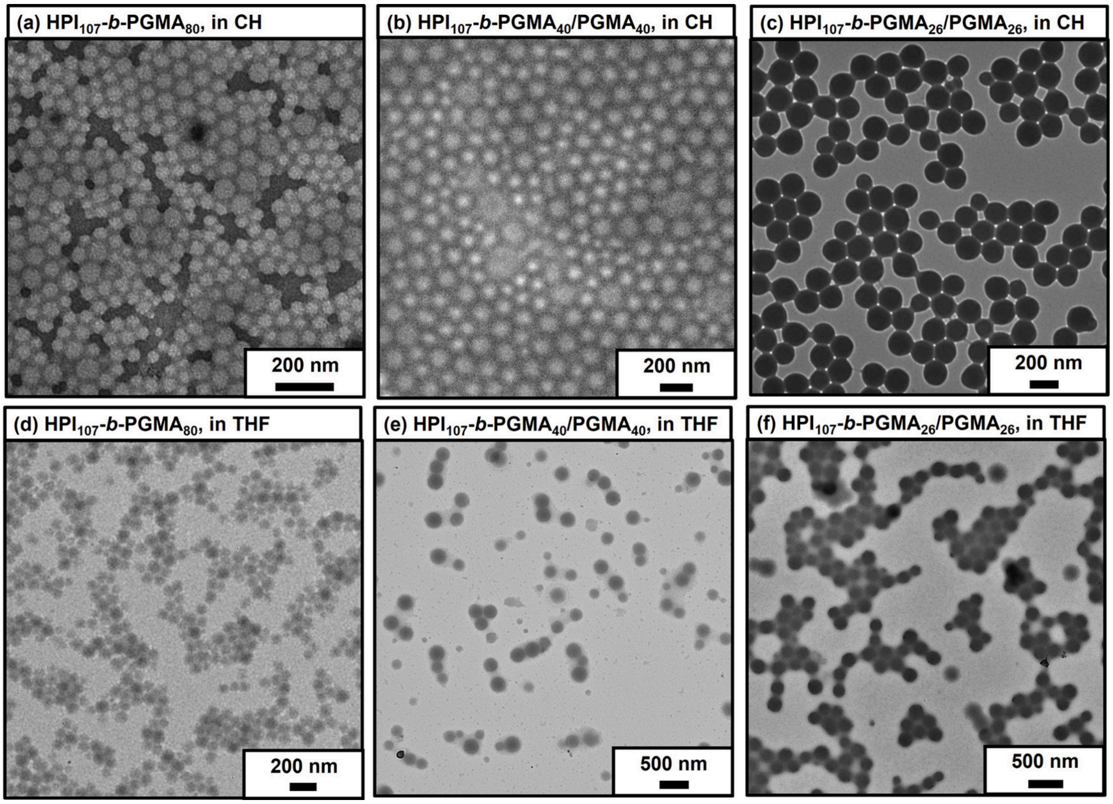

Fig. 2. TEM images of HPI-*b*-PGMA/PGMA based nano-objects formed in ARGET ATRP PISA process using the HPI-Br as macroinitiator, EBiB as small molecular initiator, solids content of 20% *w/w*, wt_{PGMA}/wt_{HPI} ratio of 1.47, and different $[EBiB]_0/[HPI\text{-}Br]_0$ ratios of (a, d) 0, (b, e) 1.0, (c, f) 2.0, diluted into 0.1%–1% *w/w* in cyclohexane (CH) or tetrahydrofuran (THF), respectively.

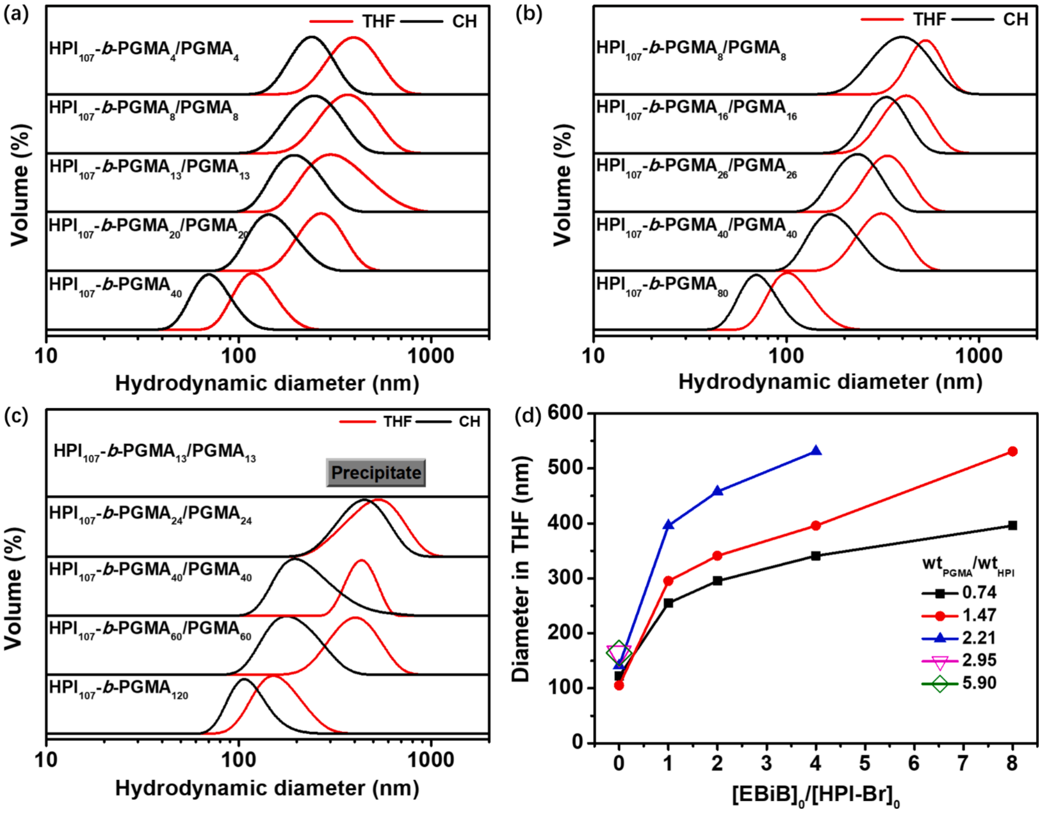

Fig. 3. DLS traces for HPI-*b*-PGMA/PGMA based nano-objects in tetrahydrofuran (THF, red curves) or cyclohexane (CH, black curves) after the precipitation (diluted into 0.1% *w/w*).

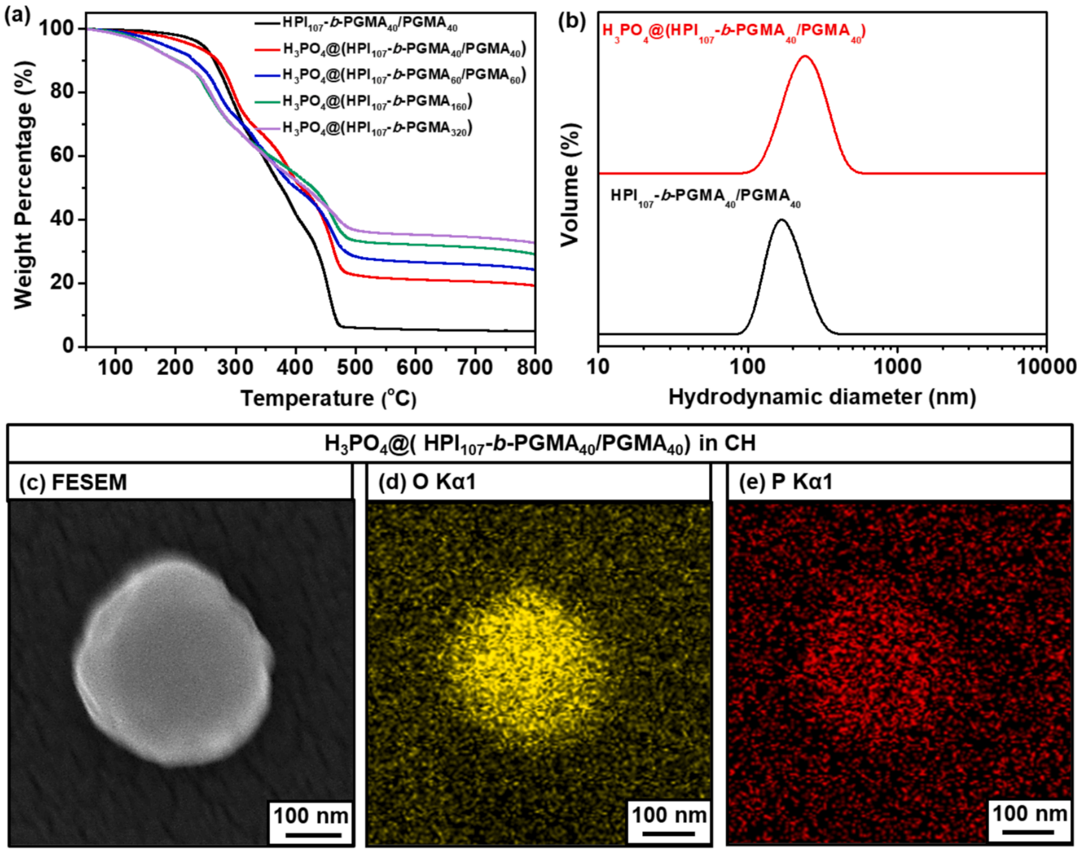

Fig. 4. (a) TGA curves for HPI_{107}-*b*-$PGMA_{40}$/$PGMA_{40}$, H_3PO_4@(HPI-*b*-PGMA) and H_3PO_4@(HPI-*b*-PGMA/PGMA) nano-objects under nitrogen atmosphere. (b) DLS traces for HPI_{107}-*b*-$PGMA_{40}$/$PGMA_{40}$ and H_3PO_4@(HPI_{107}-*b*-$PGMA_{40}$/$PGMA_{40}$) nano-objects in cyclohexane (CH). (c) FESEM images of H_3PO_4@(HPI_{107}-*b*-$PGMA_{40}$/$PGMA_{40}$), and (d, e) EDS mapping images for O and P elements.

(–C*H*$_2$=C*H*–) on the GMA monomer completely disappeared, indicating complete conversion of the GMA monomer in all ARGET ATRP PISA process (**Fig. S5**).

As an example, the morphologies and sizes of the nano-objects were examined by TEM measurement with a fixed wt_{PGMA}/wt_{HPI} ratio of 1.47, while with a varied $[EBiB]_0/[HPI\text{-}Br]_0$ ratio. When $[EBiB]_0/[HPI\text{-}Br]_0$ ratio was set as 0, the PISA process in cyclohexane generated the HPI_{107}-*b*-$PGMA_{80}$ based spherical nano-objects with an average diameter around 68 nm (Fig. 2**a**). When $[EBiB]_0/[HPI\text{-}Br]_0$ ratio was increased as 1.0, the HPI_{107}-*b*-$PGMA_{40}$/$PGMA_{40}$ based spherical nano-objects with larger sizes around 164 nm were captured (Fig. 2**b**). When $[EBiB]_0/[HPI\text{-}Br]_0$ ratio was increased as 2.0, sizes of the HPI_{107}-*b*-$PGMA_{26}$/$PGMA_{26}$ based spherical nano-objects increased to 220 nm (Fig. 2**c**). Continuously, when $[EBiB]_0/[HPI\text{-}Br]_0$ ratio was increased as 4.0 and 8.0, the sizes of HPI_{107}-*b*-$PGMA_{16}$/$PGMA_{16}$ and HPI_{107}-*b*-$PGMA_{8}$/$PGMA_{8}$ based spherical nano-objects increased to 341 nm and 396 nm, respectively (**Fig. S6a** and **Fig. S6b**). Accompanying with the PISA process, the oxirane groups underwent *in-situ* crosslinking in the presence of the $Sn(Oct)_2$ agent. As THF is a good solvent for both HPI and PGMA blocks, the successful stabilization of the nano-objects in THF was further confirmed by TEM measurement. As shown in Fig. 2**d-2f**, **Fig. S6c and Fig. S6d,** the spheres with sizes of 105 nm, 295 nm, 341 nm, 396 nm, and 531 nm were observed by TEM measurement. Obviously, the nano-objects retained the regular spherical morphologies in THF solvent, confirming the successful stabilization during the PISA process.

Alternatively, the DLS curves showed unimodal size distributions for all nano-objects (Fig. 3**a-3c**). Generally, the diameters of the nano-objects in THF were slightly larger than those in cyclohexane, which could be attributed to the stronger swelling effect of THF on the nano-objects than that of cyclohexane. The DLS results indicated that both the wt_{PGMA}/wt_{HPI} and $[EBiB]_0/[HPI\text{-}Br]_0$ ratios comprehensively affected the size evolution of nano-objects. As shown in Fig. 3**d**, higher wt_{PGMA}/wt_{HPI} and $[EBiB]_0/[HPI\text{-}Br]_0$ ratios led to the formation of larger spherical nano-objects. The formation of nano-objects in our system followed a mechanism similar to a typical PICA process reported in the literature [23]. Taking the formation of HPI_{107}-*b*-$PGMA_{24}$/$PGMA_{24}$ nano-objects as an example. The ARGET ATRP PISA system involved initiation from a homogeneous solution containing EBiB and HPI-Br initiator, and GMA monomer, resulting in the simultaneous chain growth of both homopolymer and block copolymer. The homopolymer gradually reached its solubility limit and formed nascent aggregates, *i.e.,* nucleation, which were subsequently adsorbed by the gradually chain-extended HPI_{107}-*b*-$PGMA_x$ ($x < 24$) block copolymer. The nano-objects, consisting of "living" homopolymer and block copolymer, continued to grow in the core region until the GMA monomer was completely consumed. The PGMA homopolymers were finally encapsulated and stabilized into the micelles. This led to a uniform distribution of the homopolymer within the core of the final nano-objects. During the PISA process, it should be noted that HPI_{107}-*b*-$PGMA_x$ ($x < 24$) acted as a surfactant, which could be readily, dynamically desorbed and absorbed onto the nano-objects due to the relatively lower DP of PGMA block ($x < 24$). Thus, the nano-objects could grow into larger sizes by continuously absorbing homopolymer and block copolymer, and correspondingly, the number of nucleated objects was finally reduced. Alternatively, in the case of HPI_{107}-*b*-$PGMA_{120}$ nano-objects, the HPI_{107}-*b*-$PGMA_x$ ($x < 120$) itself formed the aggregates and nucleation. At a certain point, the block copolymer was seriously entangled and difficult to rearrange due to the formation of PGMA block with a relatively higher DP. Correspondingly, the number of nucleated objects

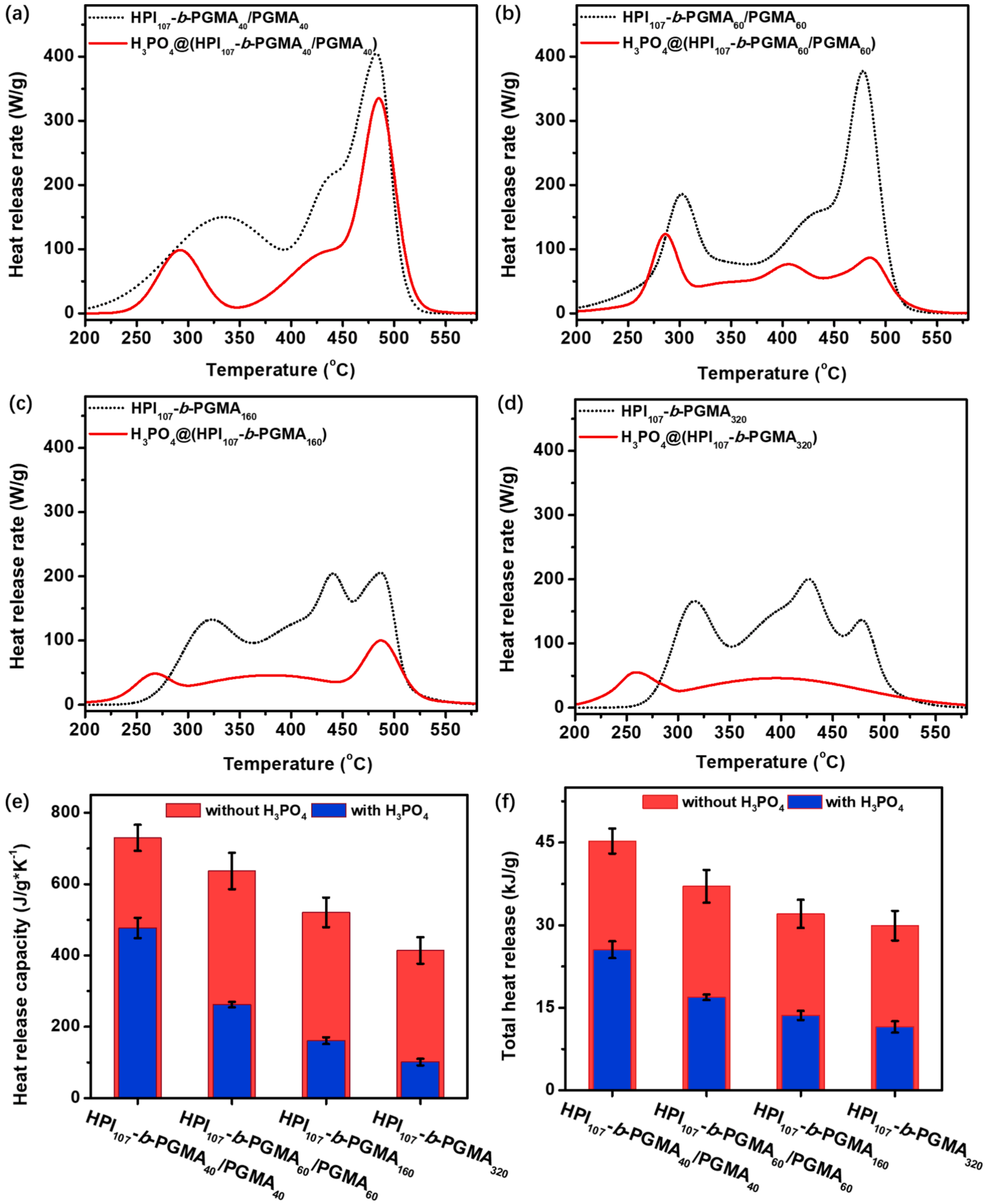

Fig. 5. MCC curves for (a) HPI_{107}-*b*-$PGMA_{40}/PGMA_{40}$ and H_3PO_4@(HPI_{107}-*b*-$PGMA_{40}/PGMA_{40}$), (b) HPI_{107}-*b*-$PGMA_{60}/PGMA_{60}$ and H_3PO_4@(HPI_{107}-*b*-$PGMA_{60}/PGMA_{60}$), (c) HPI_{107}-*b*-$PGMA_{160}$ and H_3PO_4@(HPI_{107}-*b*-$PGMA_{160}$), (d) HPI_{107}-*b*-$PGMA_{320}$ and H_3PO_4@(HPI_{107}-*b*-$PGMA_{320}$), and comparison of (e) HRC, (f) THR results.

remained constant. The remaining GMA monomer in the core region was finally polymerized and the nano-objects with relatively smaller sizes were kept. Of course, with the variation of $[EBiB]_0/[HPI\text{-}Br]_0$ and the corresponding DP of PGMA homopolymer, the sizes could be elaborately modulated.

3.3. *Preparation of H_3PO_4-containing nano-objects by ring-opening reaction*

The efficient ring-opening reaction between oxirane and H_3PO_4 enabled the incorporation of H_3PO_4 into the core region of HPI-*b*-PGMA or HPI-*b*-PGMA/PGMA nano-objects. The purified H_3PO_4@(HPI-*b*-PGMA) or H_3PO_4@(HPI-*b*-PGMA/PGMA) nano-objects were first characterized by thermogravimetric analysis (TGA). As shown in Fig. 4**a**, with the increase of wt_{PGMA}/wt_{HPI} ratios from H_3PO_4@(HPI_{107}-*b*-$PGMA_{40}$/$PGMA_{40}$) to H_3PO_4@(HPI_{107}-*b*-$PGMA_{60}$/$PGMA_{60}$), H_3PO_4@(HPI_{107}-*b*-$PGMA_{160}$) and H_3PO_4@(HPI_{107}-*b*-$PGMA_{320}$), the residual mass attributed to H_3PO_4 increased steadily within the temperature range of 500–800 ℃. This trend indicated that a higher PGMA content facilitated the introduction of a higher amount of H_3PO_4. As a comparison, the residual mass of H_3PO_4@(HPI_{107}-*b*-$PGMA_{40}$/$PGMA_{40}$) was significantly higher than that of HPI_{107}-*b*-$PGMA_{40}$/$PGMA_{40}$. Meanwhile, the DLS results showed that the H_3PO_4@(HPI_{107}-*b*-$PGMA_{40}$/$PGMA_{40}$) nano-objects exhibited a slightly larger size compared to HPI_{107}-*b*-$PGMA_{40}$/$PGMA_{40}$ (Fig. 4**b**), which could be attributed to the introduction of H_3PO_4 into the PGMA core. To validate the successful incorporation of H_3PO_4 into the nano-objects, the H_3PO_4@(HPI_{107}-*b*-$PGMA_{40}$/$PGMA_{40}$) nano-objects were further examined by field emission scanning electron microscope (FESEM) and energy dispersive spectrometer (EDS) measurements (Fig. 4**c-4e**). It could be clearly observed that the oxygen (O) and phosphorus (P) elements were successfully introduced into the nano-objects. Thus, the TGA, DLS, and FESEM results comprehensively confirmed the successful preparation of targeted H_3PO_4@(HPI-*b*-PGMA) or H_3PO_4@(HPI-*b*-PGMA/PGMA) nano-objects.

3.4. Flame retardancy of H_3PO_4-containing nano-objects

According to the literatures [42,43,44], the presence of phosphorus compounds (e.g., phosphine oxides, phosphorus heterocyclic compounds, H_3PO_4, etc.) could improve the flame retardancy of materials by forming a protective char layer through thermal decomposition. This process promotes the dehydration and carbonization of polymers, effectively isolating heat and oxygen. Herein, the flame-retardant potential of the nano-objects was evaluated using the microscale combustion calorimetry (MCC) method, a widely employed technique for assessing the flammability of polymeric materials by analyzing the combustion of pyrolyzed products [45,46,47,48]. Typically, the MCC method determines key flammability metrics, such as peak heat release rate (pHRR), heat release capacity (HRC), and total heat release (THR), based on parameters including oxygen consumption, heating rate, flow rate, and sample weight [49]. As shown in Fig. 5**a-5d**, the MCC curves of HPI_{107}-*b*-$PGMA_{40}$/$PGMA_{40}$, HPI_{107}-*b*-$PGMA_{60}$/$PGMA_{60}$, HPI_{107}-*b*-$PGMA_{160}$, and HPI_{107}-*b*-$PGMA_{320}$ nano-objects, as well as the phosphorylated samples, were recorded and analyzed.

The pHRR, THR and HRC results of the samples were further derived from MCC measurements and presented in **Table S1**. Compared with the HPI_{107}-*b*-$PGMA_{40}$/$PGMA_{40}$, HPI_{107}-*b*-$PGMA_{60}$/$PGMA_{60}$, HPI_{107}-*b*-$PGMA_{160}$, and HPI_{107}-*b*-$PGMA_{320}$, the HRC of H_3PO_4@(HPI_{107}-*b*-$PGMA_{40}$/$PGMA_{40}$), H_3PO_4@(HPI_{107}-*b*-$PGMA_{60}$/$PGMA_{60}$), H_3PO_4@(HPI_{107}-*b*-$PGMA_{160}$), and H_3PO_4@(HPI_{107}-*b*-$PGMA_{320}$) nano-objects decreased by 35 %, 58 %, 69 % and 75 %, while the THR decreased by 43 %, 54 %, 57 %, and 61 %, respectively (Fig. 5**e-5f**). Similarly, the pHRR of the H_3PO_4-functionalized nano-objects decreased by 18 %, 66 %, 50 %, and 72 %, respectively (**Fig. S7**). Obviously, as the DP_{PGMA} and H_3PO_4 content increased, the THR, HRC, and pHRR were consistently reduced, indicating a clear correlation between H_3PO_4 loading and improved flame retardancy. Moreover, the purified and recovered H_3PO_4@(HPI-*b*-PGMA) and H_3PO_4@(HPI-*b*-PGMA/PGMA) nano-objects stabilized by the low polar, nano-crystallizable HPI block demonstrated excellent dispersity in low polar cyclohexane during a long-term (**Fig. S8**), allowing them to be well-dispersed in the PO matrix, such as the non-crystallizable POE or EPDM, *etc*. These properties suggested that the developed nano-objects might hold great potential as effective additives in the PO industry.

4. CONCLUSIONS

In summary, the ARGET ATRP PISA process was successfully employed to synthesize the HPI-*b*-PGMA/PGMA based nano-objects by varying the wt_{PGMA}/wt_{HPI} and $[EBiB]_0/[HPI\text{-}Br]_0$ ratios, and the hydrodynamic diameters of the spherical nano-objects were effectively modulated. The H_3PO_4 was introduced into the PGMA core and their flame retardancy was evaluated, highlighting their potential as novel PO-based additives. Especially, due to the presence of the low polar, non-crystallizable PO shell, the PO-functionalized spheres offered distinct advantages in dispersing in low polar cyclohexane and compatibility with low polar PO matrix, such as non-crystallizable POE or EPDM, *etc*. It is proposed that HPI-*b*-PGMA/PGMA based nano-objects will significantly improve the function of additives and broaden the application scope in PO industry.

CRediT authorship contribution statement

Xinyue Liang: Writing – review & editing, Writing – original draft, Validation, Methodology, Investigation, Formal analysis, Data curation, Conceptualization. **Jingwei Zhang:** Writing – review & editing, Validation, Formal analysis. **Xiaoxiao Wu:** Validation, Formal analysis. **Xiaotong Fang:** Validation, Formal analysis. **Pengyu Qu:** Validation. **Guowei Wang:** Writing – review & editing, Supervision, Resources, Project administration, Methodology, Funding acquisition, Conceptualization.

Declaration of competing interest

The authors declare the following financial interests/personal relationships which may be considered as potential competing interests: [Guowei Wang reports financial support was provided by the National Natural Science Foundation of China. If there are other authors, they declare that they have no known competing financial interests or personal relationships that could have appeared to influence the work reported in this paper.].

Acknowledgements

We appreciate the financial support of this research by the National Natural Science Foundation of China (22271058).

Appendix A. Supplementary data

Supplementary data to this article can be found online at https://doi.org/10.1016/j.eurpolymj.2025.113906.

Data availability

Data will be made available on request.

References

[1] M. Atiqullah, H.S. Al-Asiri, Polyolefin catalyst research: a product-driven industrial perspective, Chem. Rec., 22 (7) (2022) 202100321, https://doi.org/10.1002/tcr.202100321.
[2] X.-Y. Wang, Y. Gao, Y. Tang, Sustainable developments in polyolefin chemistry: progress, challenges, and outlook, Prog. Polym. Sci., 143 (2023) 101713, https://doi.org/10.1016/j.progpolymsci.2023.101713.
[3] L. Emhofer, C.W. Klampfl, W. Buchberger, A fast and simple method for the analysis of polymer stabilizers migrating from polyolefin foils using large-volume-Injection HPLC with UV and mass-spectrometric detection, Curr. Anal. Chem., 12 (2) (2016) 108–112, https://doi.org/10.2174/1573411011666150724225715.
[4] M. Lundback, M.S. Hedenqvist, A. Mattozzi, U.W. Gedde, Migration of phenolic antioxidants from linear and branched polyethylene, Polym. Degrad. Stab., 91 (7) (2006) 1571–1580, https://doi.org/10.1016/j.polymdegradstab.2005.09.008.
[5] A.S. Silva, R.S. García, I. Cooper, R. Franz, P.P. Losada, Compilation of analytical methods and guidelines for the determination of selected model migrants from plastic packaging, Trends Food Sci. Technol. 17 (10) (2006) 535–546, https://doi.org/10.1016/j.tifs.2006.04.009.
[6] Z. Balzade, F. Sharif, S.R.G. Anbaran, Tailor-made functional polyolefins of complex architectures: recent advances, applications, and prospects, Macromolecules 55 (16) (2022) 6938–6972, https://doi.org/10.1021/acs.macromol.2c00594.

[7] A. Bunescu, S. Lee, Q. Li, J.F. Hartwig, Catalytic hydroxylation of polyethylenes, ACS Cent. Sci., 3 (8) (2017) 895–903, https://doi.org/10.1021/acscentsci.7b00255.
[8] J. Gao, W. Cai, Y. Hu, C. Chen, Improving the flame retardancy of polyethylenes through the palladium-catalyzed incorporation of polar comonomers, Polym. Chem., 10 (12) (2019) 1416–1422, https://doi.org/10.1039/c8py01772g.
[9] C. Zou, C. Chen, Polar-functionalized, crosslinkable, self-healing, and photoresponsive polyolefins, Angew. Chem. Int. Ed., 59 (1) (2020) 395–402, https://doi.org/10.1002/anie.201910002.
[10] L. Jasinska-Walc, M. Bouyahyi, R. Duchateau, Potential of functionalized polyolefins in a sustainable polymer economy: synthetic strategies and applications, Acc. Chem. Res. 55 (15) (2022) 1985–1996, https://doi.org/10.1021/acs.accounts.2c00195.
[11] N.J. Warren, S.P. Armes, Polymerization-induced self-assembly of block copolymer nano-objects via RAFT aqueous dispersion polymerization, J. Am. Chem. Soc., 136 (29) (2014) 10174–10185, https://doi.org/10.1021/ja502843f.
[12] A. Blanazs, A.J. Ryan, S.P. Armes, Predictive phase diagrams for RAFT aqueous dispersion polymerization: effect of block copolymer composition, molecular weight, and copolymer concentration, Macromolecules 45 (12) (2012) 5099–5107, https://doi.org/10.1021/ma301059r.
[13] G. Delaittre, C. Dire, J. Rieger, J.L. Putaux, B. Charleux, Formation of polymer vesicles by simultaneous chain growth and self-assembly of amphiphilic block copolymers, Chem. Commun. (20) (2009) 2887–2889, https://doi.org/10.1039/b903040a.
[14] E. Groison, S. Brusseau, F. D'Agosto, S. Magnet, R. Inoubli, L. Couvreur, B. Charleux, Well-defined amphiphilic block copolymer nanoobjects via nitroxide-mediated emulsion polymerization, ACS Macro. Lett., 1 (1) (2012) 47–51, https://doi.org/10.1021/mz200035b.
[15] G. Wang, M. Schmitt, Z.Y. Wang, B. Lee, X.C. Pan, L.Y. Fu, J.J. Yan, S.P. Li, G.J. Xie, M.R. Bockstaller, K. Matyjaszewski, Polymerization-induced self-assembly (PISA) using ICAR ATRP at low catalyst concentration, Macromolecules 49 (22) (2016) 8605–8615, https://doi.org/10.1021/acs.macromol.6b01966.
[16] J. Kim, S.Y. Jeong, K.U. Kim, Y.H. Ahn, R.P. Quirk, Anionic dispersion polymerization.1. control of particle size, J. Polym. Sci., Part A: Polym. Chem. 34 (16) (1996) 3277–3288, https://doi.org/10.1002/(SICI)1099-0518(19961130)34:16<3277::AID-POLA3>3.0.CO;2-R.
[17] J. Wang, M. Cao, P. Zhou, G. Wang, Exploration of a living anionic polymerization mechanism into polymerization-induced self-assembly and site-specific stabilization of the formed nano-objects, Macromolecules 53 (8) (2020) 3157–3165, https://doi.org/10.1021/acs.macromol.0c00371.
[18] J. Liu, Y. Liao, X. He, J. Yu, L. Ding, M. Xie, Facile one-pot approach for preparing functionalized polymeric nanoparticles via ROMP, Macromol. Chem. Phys., 212 (1) (2011) 55–63, https://doi.org/10.1002/macp.201000416.
[19] D.B. Wright, M.A. Touve, L. Adamiak, N.C. Gianneschi, ROMPISA: ring-opening metathesis polymerization-induced self-assembly, ACS Macro. Lett., 6 (9) (2017) 925–929, https://doi.org/10.1021/acsmacrolett.7b00408.
[20] S.L. Canning, G.N. Smith, S.P. Armes, A critical appraisal of RAFT-mediated polymerization-induced self assembly, Macromolecules 49 (6) (2016) 1985–2001, https://doi.org/10.1021/acs.macromol.5b02602.
[21] C. Gyorgy, S.P. Armes, Recent advances in polymerization-induced self-assembly (PISA) syntheses in non-polar media, Angew. Chem. Int. Ed. 62 (42) (2023) 202308372, https://doi.org/10.1002/anie.202308372.
[22] Q. Gu, H. Li, E.J. Cornel, J. Du, New driving forces and recent advances in polymerization-induced self-assembly, Cell Rep. Phys. Sci., 4 (7) (2023) 101495, https://doi.org/10.1016/j.xcrp.2023.101495.
[23] A. Zhu, X. Lv, L. Shen, B. Zhang, Z. An, Polymerization-induced cooperative assembly of block copolymer and homopolymer via RAFT dispersion polymerization, ACS Macro. Lett., 6 (3) (2017) 304–309, https://doi.org/10.1021/acsmacrolett.7b00069.
[24] J. Zhang, P. Zhou, B. Shi, P. Li, G. Wang, High-efficient access to inverse morphologies via living anionic polymerization-mediated polymerization-induced cooperative assembly, Macromolecules 56 (15) (2023) 5743–5753, https://doi.org/10.1021/acs.macromol.3c00759.
[25] B. Yuan, X. He, Y. Qu, C. Gao, E. Eiser, W. Zhang, In situ synthesis of a self-assembled AB/B blend of poly(ethylene glycol)-b-polystyrene/polystyrene by dispersion RAFT polymerization, Polym. Chem., 8 (14) (2017) 2173–2181, https://doi.org/10.1039/c7py00339k.
[26] J.N. Israelachvili, D.J. Mitchell, B.W. Ninham, Theory of self-assembly of hydrocarbon amphiphiles into micelles and bilayers, J. Chem. Soc., Faraday Trans. 2 (72) (1976) 1525–1568, https://doi.org/10.1039/f29767201525.
[27] S. Li, G. Han, W. Zhang, Cross-linking approaches for block copolymer nano-assemblies via RAFT-mediated polymerization-induced self-assembly, Polym. Chem., 11 (29) (2020) 4681–4692, https://doi.org/10.1039/d0py00627k.
[28] W. Zhang, J. Kadirkhanov, C. Wang, S. Ding, C. Hong, F. Wang, Y. You, Polymerization-induced self-assembly for the fabrication of polymeric nano-objects with enhanced structural stability by cross-linking, Polym. Chem., 11 (22) (2020) 3654–3672, https://doi.org/10.1039/d0py00368a.
[29] C. Bergerbit, F. Baffie, A. Wolpers, P.Y. Dugas, O. Boyron, M. Taam, M. Lansalot, V. Monteil, F. D'Agosto, Ethylene polymerization-induced self-assembly (PISA) of poly(ethylene oxide)-block-polyethylene copolymers via RAFT, Angew. Chem. Int. Ed., 59 (26) (2020) 10385–10390, https://doi.org/10.1002/anie.202001741.
[30] N. Baulu, M. Langlais, P.-Y. Dugas, J. Thuilliez, F. Jean-Baptiste-dit-Dominique, M. Lansalot, C. Boisson, F. D'Agosto, Ethylene-coordinative chain-transfer polymerization-induced self-assembly (CCTPISA), Chem. Eur. J. 28 (60) (2022) 202202089, https://doi.org/10.1002/chem.202202089.
[31] C. Feng, X. Huang, Polymer brushes: efficient synthesis and applications, Acc. Chem. Res., 51 (9) (2018) 2314–2323, https://doi.org/10.1021/acs.accounts.8b00307.
[32] D. Tao, Z. Wang, X. Huang, M. Tian, G. Lu, I. Manners, M.A. Winnik, C. Feng, Continuous and segmented semiconducting fiber-like nanostructures with spatially selective functionalization by living crystallization-driven self-assembly, Angew. Chem. Int. Ed., 59 (21) (2020) 8232–8239, https://doi.org/10.1002/anie.202000327.
[33] F. Huang, J. Ma, J. Nie, B. Xu, X. Huang, G. Lu, M.A. Winnik, C. Feng, A versatile strategy toward donor-acceptor nanofibers with tunable length/composition and enhanced photocatalytic activity, J. Am. Chem. Soc., 146 (36) (2024) 25137–25150, https://doi.org/10.1021/jacs.4c08415.
[34] J. Schmelz, M. Karg, T. Hellweg, H. Schmalz, General pathway toward crystalline-core micelles with tunable morphology and corona segregation, ACS Nano 5 (12) (2011) 9523–9534, https://doi.org/10.1021/nn202638t.
[35] B. Darmau, M.J. Rymaruk, N.J. Warren, R. Bening, S.P. Armes, RAFT dispersion polymerization of benzyl methacrylate in non-polar media using hydrogenated polybutadiene as a steric stabilizer block, Polym. Chem., 11 (47) (2020) 7533–7541, https://doi.org/10.1039/d0py01371d.
[36] J. Wang, Z. Wu, G. Wang, K. Matyjaszewski, In situ crosslinking of nanoparticles in polymerization-induced self-assembly via ARGET ATRP of glycidyl methacrylate, Macromol. Rapid Commun. 40 (2) (2019) 1800332, https://doi.org/10.1002/marc.201800332.
[37] S.B. Luk, A. Metafiot, J. Morize, E. Edeh, M. Maric, Hydrogenation of poly (myrcene) and poly(farnesene) using diimide reduction at ambient pressure, J. Polym. Sci., 59 (19) (2021) 2140–2153, https://doi.org/10.1002/pol.20210479.
[38] N. Ouarti, P. Viville, R. Lazzaroni, E. Minatti, M. Schappacher, A. Deffieux, R. Borsali, Control of the morphology of linear and cyclic PS-b-PI block copolymer micelles via PS addition, Langmuir 21 (4) (2005) 1180–1186, https://doi.org/10.1021/la048944f.
[39] L.F. Zhang, A. Eisenberg, Multiple morphologies and characteristics of "crew-cut" micelle-like aggregates of polystyrene-b-poly(acrylic acid) diblock copolymers in aqueous solutions, J. Am. Chem. Soc. 118 (13) (1996) 3168–3181, https://doi.org/10.1021/ja953709s.
[40] N.V. Tsarevsky, W. Jakubowski, Atom transfer radical polymerization of functional monomers employing Cu-based catalysts at low concentration: polymerization of glycidyl methacrylate, J. Polym. Sci., Part A: Polym. Chem. 49 (4) (2011) 918–925, https://doi.org/10.1002/pola.24503.
[41] S.R. Woodruff, B.J. Davis, N.V. Tsarevsky, Epoxides as reducing agents for low-catalyst concentration atom transfer radical polymerization, Macromol. Rapid Commun., 35 (2) (2014) 186–192, https://doi.org/10.1002/marc.201300696.
[42] B. Liu, H. Zhao, Y. Wang, Advanced flame-retardant methods for polymeric materials, Adv. Mater. 34 (46) (2022) 2107905, https://doi.org/10.1002/adma.202107905.
[43] M.M. Velencoso, A. Battig, J.C. Markwart, B. Schartel, F.R. Wurm, Molecular firefighting-how modern phosphorus chemistry can help solve the challenge of flame retardancy, Angew. Chem. Int. Ed., 57 (33) (2018) 10450–10467, https://doi.org/10.1002/anie.201711735.
[44] X. Yang, C. Wang, J. Xia, W. Mao, S. Li, Study on synthesis of novel phosphorus-containing flame retardant epoxy curing agents from renewable resources and the comprehensive properties of their combined cured products, Prog. Org. Coat., 110 (2017) 195–203, https://doi.org/10.1016/j.porgcoat.2017.01.012.
[45] P.M. Hergenrother, C.M. Thompson, J.G. Smith, J.W. Connell, J.A. Hinkley, R. E. Lyon, R. Moulton, Flame retardant aircraft epoxy resins containing phosphorus, Polymer 46 (14) (2005) 5012–5024, https://doi.org/10.1016/j.polymer.2005.04.025.
[46] R.E. Lyon, R.N. Walters, Pyrolysis combustion flow calorimetry, J. Anal. Appl. Pyrolysis 71 (1) (2004) 27–46, https://doi.org/10.1016/s0165-2370(03)00096-2.
[47] R.E. Lyon, R.N. Walters, S.I. Stoliarov, Screening flame retardants for plastics using microscale combustion calorimetry, Polym. Eng. Sci., 47 (10) (2007) 1501–1510, https://doi.org/10.1002/pen.20871.
[48] Q. Xu, R.A. Mensah, C. Jin, L. Jiang, A critical review of the methods and applications of microscale combustion calorimetry for material flammability assessment, J. Therm. Anal. Calorim., 147 (11) (2022) 6001–6013, https://doi.org/10.1007/s10973-021-10963-4.
[49] C.Q. Yang, Q. He, R.E. Lyon, Y. Hu, Investigation of the flammability of different textile fabrics using micro-scale combustion calorimetry, Polym. Degrad. Stab., 95 (2) (2010) 108–115, https://doi.org/10.1016/j.polymdegradstab.2009.11.047.